SCIENTIFIC REPORTS

OPEN

Uniform Nickel Vanadate ($Ni_3V_2O_8$) Nanowire Arrays Organized by Ultrathin Nanosheets with Enhanced Lithium Storage Properties

Chang Wang[1], Dong Fang[1], Hong'en Wang[2], Yunhe Cao[1], Weilin Xu[1], Xiaoqing Liu[2], Zhiping Luo[3], Guangzhong Li[4], Ming Jiang[1] & Chuanxi Xiong[1,2]

Development of three-dimensional nano-architectures on current collectors has emerged as an effective strategy for enhancing rate capability and cycling stability of the electrodes. Herein, a novel type of $Ni_3V_2O_8$ nanowires, organized by ultrathin hierarchical nanosheets (less than 5 nm) on Ti foil, has been obtained by a two-step hydrothermal synthesis method. Studies on structural and thermal properties of the as-prepared $Ni_3V_2O_8$ nanowire arrays are carried out and their morphology has changed obviously in the following heat treatment at 300 and 500 °C. As an electrode material for lithium ion batteries, the unique configuration of $Ni_3V_2O_8$ nanowires presents enhanced capacitance, satisfying rate capability and good cycling stability. The reversible capacity of the as-prepared $Ni_3V_2O_8$ nanowire arrays reaches 969.72 mAh·g^{-1} with a coulombic efficiency over 99% at 500 mA·g^{-1} after 500 cycles.

Energy conversion and storage is undoubtedly one of the greatest challenges in today's world[1]. Lithium ion batteries (LIBs) are deemed among the best choices owing to their high specific energy and long cycle life in portable electronic consumer devices, electric vehicles, and large-scale electricity storage in intelligent grids[2–4]. It has led the extensive research efforts on the development of electrode materials with higher specific capacity. In particular, the materials that store lithium ions (Li$^+$ ions) through conversion reactions (such as MnO_2[5], Co_3O_4[6], V_2O_5[7]) or alloying reactions (such as Si[8], Sn[1]) have been suggested as promising alternative materials due to their intrinsically high specific capacity. However, one drawback exists for commercially available LIBs electrode materials due to the intrinsic diffusivity of Li$^+$ ions in the solid state (about 10^{-8} cm^2 s^{-1}), which unavoidably limits the charge/discharge performance[9,10]. Further, these materials typically undergo significant volume change during lithiation and delithiation due to the large Li atoms uptake in the structure and accompanying phase transformation. Approaches for enhancing ion/electron transport kinetics and accommodate strain induced by volume change in LIBs include coating electrolytically active material with a conductive layer[11–13]. Designing the electrode materials with nanoscale features is an alternative useful method because nanostructures can help to reduce the diffusion length for Li$^+$ ions during the charge/discharge process and increase the interfacial contact area between electrode and electrolyte, thus leading to significantly enhanced specific power density and energy density as compared with non-nanostructure materials[14–19]. Hierarchical structure materials with at least one dimension on the nanometer length scale (hierarchical nanostructures) can combine desirable bulk-material properties (such as structural stability and high tap density) with size-tunable functional properties for the construction of electrochemical energy storage devices (LIBs and supercapacitors)[20,21].

[1]Key Lab of Green Processing and Functional Textiles of New Textile Materials, Ministry of Education, College of Material Science and Engineering, Wuhan Textile University, Wuhan 430070, China. [2]School of Materials Science and Engineering, Wuhan University of Technology, Wuhan 430070, China. [3]Department of Chemistry and Physics, Fayetteville State University, Fayetteville, USA. [4]State Key Laboratory of Porous Metal Material, Northwest Institute for Non-ferrous Metal Research, Xi'an 710000, China. Correspondence and requests for materials should be addressed to D.F. (email: csufangdong@gmail.com) or W.L.X. (Email: weilin_xu@hotmail.com)
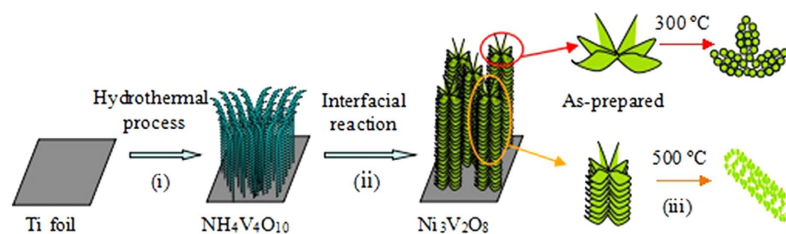
Figure 1. Schematic illustration of the formation process of $Ni_3V_2O_8$ nanowire arrays: (**i**) formation of $NH_4V_4O_{10}$ nanowire arrays on the surface of the Ti foil, (**ii**) further growth of $Ni_3V_2O_8$ nanowire arrays organized by ultrathin nanosheets, and (**iii**) formation of porous structure through calcinations.

Nickel oxide (NiO), a base transition metal oxide enriched in nature resources with environmental benignity, has been considered as one of the fascinated electrode materials for lithium storage[22–25]. The main challenges to implement NiO based anodes are their low electronic conductivity and large volume change during lithium insertion and extraction as mentioned above. To address these issues, binary metal oxides, such as $NiMn_2O_4$[26], and $NiCo_2O_4$[27], have also been proposed as anode materials to improve their electrochemical performances. In this case, the binary metal oxides have much higher electrical conductivity and electrochemical performances than single oxide[27,28]. The higher electronic conductivity is favorable for the rapid transfer of electrons in an electrode. Recently, transition metal vanadates (MV_xO_y), which are related to V_2O_5 with tunable oxidation states (V^{5+}, V^{4+} and V^{3+}), have received increasing attention for potential applications in various fields due to their layered structure, unique physical, chemical, and electrical properties[7,29]. The electrode cycling stability of pure vanadium oxides has been greatly improved by addition of M (=Li, Fe, Cr, or Na) ions into these host vanadium oxides, such as LiV_3O_8[30], $FeVO_4$[31], $Cr_{0.11}V_2O_{5.16}$[32], $Na_5V_{12}O_{32}$[33]. These additional M ions were arranged to form pillars between the vanadium oxide layers and thus stabilized the structure during the Li^+ insertion/extraction[33,34].

In the present work, we present an efficient two-step hydrothermal synthesis method to synthesize $Ni_3V_2O_8$ nanowire arrays organized by ultrathin nanosheets. To our knowledge, $Ni_3V_2O_8$ structures such as nanowires or nanosheets have not been reported previously. Morphological evolution and phase transformations of $Ni_3V_2O_8$ nanowire arrays during the calcinations process are studied by field emission scanning electron microscopy (FE-SEM), transmission electron microscopy (TEM), and X-ray diffraction microscopy (XRD). Due to the unique properties of these nanowire arrays, such as high surface areas, crystallinity, good conductivity and direct growth on conductive substrates, they have potential applications in LIBs, chemical sensing, electrochemical or photocatalysis, field emission, and electrochromic devices[35,36]. As an electrode material for LIBs, the as-grown $Ni_3V_2O_8$ nanowires on Ti foil present outstanding energy storage properties.

Results and Discussion

The general electrode fabrication protocol is illustrated in Fig. 1. First, $NH_4V_4O_{10}$ nanowire arrays are grown directly on a Ti substrate via a facile modified hydrothermal process. The obtained almost crystalline $NH_4V_4O_{10}$ nanowire arrays are then subjected to impregnation with $C_4H_6O_4Ni$ aqueous solution for reaction, which leads to obtain $Ni_3V_2O_8$ nanowire arrays. This is enlightened by the fact that $Ni_3V_2O_8$ can be produced by the green reaction between $NH_4V_4O_{10}$ and $C_4H_6O_4Ni$, in the absence of any acid or base ($NH_4V_4O_{10} + C_4H_6O_4Ni \rightarrow Ni_3V_2O_8 + C_4H_6O_4NH_4$). Here, the ordered $NH_4V_4O_{10}$ nanowires obtained in the first step are purposely designed as an interfacial reactive template to grow $Ni_3V_2O_8$ nanowire arrays (step ii). For comparison, the as-prepared $Ni_3V_2O_8$ nanowire arrays are annealed in air, interesting, the nanosheets on the nanowires transfer to nanoparticles after heat treatment at 300 °C, and the nanowires change to porous or tubular structure after annealing at 500 °C.

The corresponding XRD patterns provide verification of the detailed structural and phase information used to index the as-obtained samples. The XRD patterns of $NH_4V_4O_{10}$ and $Ni_3V_2O_8$ after heat treatments at 300 and 500 °C are presented in Fig. S1a. The as-prepared $Ni_3V_2O_8$ obtained after hydrothermal reaction exhibits an orthorhombic structure. After heat treatment at 500 °C, the sample shows a highly crystalline nature and the whole diffraction peaks can be indexed to $Ni_3V_2O_8$ orthorhombic phase (JCPDS card No. 70-1394)[37]. No characteristic peaks, related to NiO, TiO_2, $NH_4V_4O_{10}$, or V_2O_5, are detected in the produced material, indicating pure $Ni_3V_2O_8$ nanowires on the surface of Ti substrate. Comparing the curves in Fig. S1a, it is noted that XRD peaks of the as-prepared $Ni_3V_2O_8$ are broadened. A variety of factors can be contributed to the width of a diffraction peak besides instrumental effects and crystallite size, and the most important factors are usually inhomogeneous strain and crystal lattice imperfections, or crystallinity[38,39]. From the crystal effect on diffraction by the Scherrer equation[40], the crystal size of the as-prepared $Ni_3V_2O_8$ is smaller than that of the annealed samples (see Table S1 in supporting information). Further, the XRD peaks (2θ) shift to higher values with increasing the treatment temperature. A small change in peak shift does not necessarily mean phase change. Solid solution, be it substitutional or interstitial, can cause a shift in the x-ray diffraction peaks. Another two factors which contribute to peak shift are residual stress and defects in the material, because these two factors also can deform the lattice, causing peak shift[41]. Figure S1b shows the unit cell consisting of nickel, vanadium and oxygen atoms, presenting the mixed valence oxides that crystallize in the orthorhombic system with lattice constants: $a = 5.936$ Å, $b = 11.420$ Å, and $c = 8.240$ Å. It also clearly displays the detailed structure which all nickel ions are the arrays of edge-shared NiO_6 octahedra forming Kagome-like layers, and the layers are separated by VO_4 tetrahedra, resulting in a peculiar Kagome-staircase geometry[42].
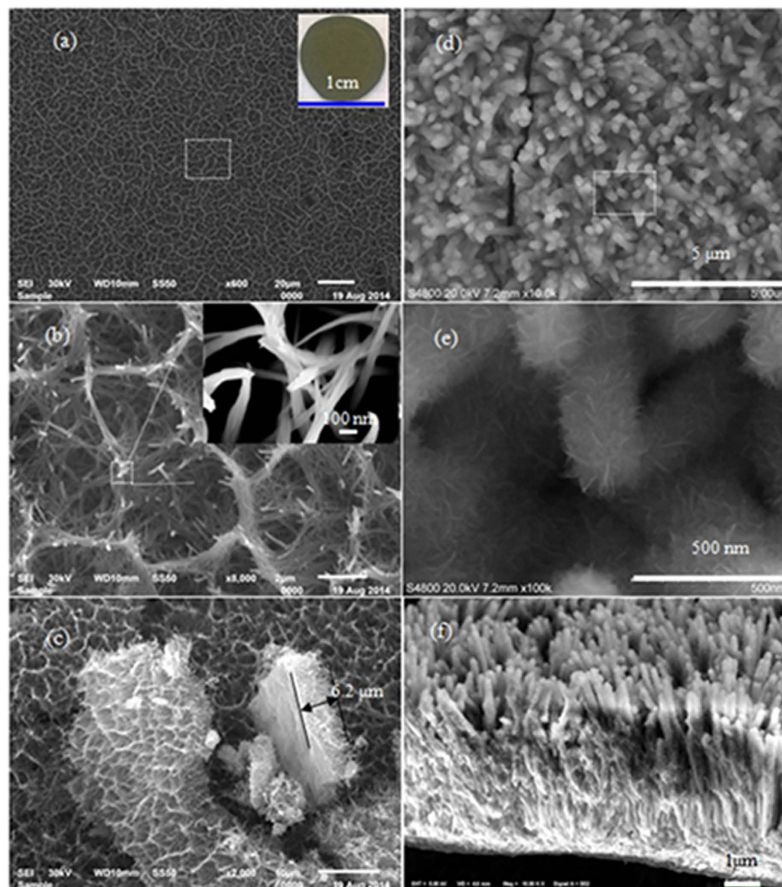
Figure 2. (**a–c**) The FE-SEM images of the $NH_4V_4O_{10}$ nanowire arrays and (**d–f**) the as-prepared $Ni_3V_2O_8$ nanowire arrays; (**a,b,d,e**) the top-view FE-SEM images; and (**c,f**) the cross-sectional FE-SEM images. The inset in (**a**) shows a digital image of the $NH_4V_4O_{10}$ nanowire arrays on Ti foil.

X-ray photoelectron spectroscopy (XPS) (see Fig. S2 in the Supplementary Information) is used to demonstrate the structure and purity of the sample. A wide-range survey XPS spectrum of the as-prepared sample reveals the presence peaks of C 1s (at $\sim$284.6 eV), V 2p (at $\sim$517.1 eV), O 1s (at $\sim$531.9 eV) and Ni 2p (at $\sim$855.8 eV) (Fig. S2a). The C 1s peak at 284.6 eV is used as a reference binding energy for calibration. After annealing up to 300 °C, the XPS spectrum in Fig. S2b is similar to that of the as-prepared $Ni_3V_2O_8$. The peak deconvolution and fittings are carried out using Gaussian-Lorentzian shaped peaks based on the Shirley background correction. Two typical peaks centered at 855.9 and 873.8 eV are observed (Fig. S2c), corresponding to spin-orbit peaks of the Ni $2p_{3/2}$ and Ni $2p_{1/2}$ of $Ni_3V_2O_8$, respectively. Meanwhile, two satellite lines associated with Ni 2p also appear. From the binding energies of Ni 2p main lines and the splitting due to the spin-orbit coupling, besides the energy gaps separating the main lines and satellite peaks, it indicates that Ni (II) and Ni (III) cations together exist in $Ni_3V_2O_8$ structures[43]. The high resolution scan of the V 2p core levels is performed in Fig. S2d, in which the peak position of V $2p_{3/2}$ is fitted using a Shirley function[44]. The V species exist with a close binding energy value of V^{5+} $2p_{3/2}$ (516.4–517.4 eV) and V^{4+} $2p_{3/2}$ (515.4–515.7 eV)[45,46]. Therefore, the peak fitted at 517.0 eV can be mainly ascribed to V^{5+} $2p_{3/2}$, whereas that at 515.6 eV is assigned to V^{4+} $2p_{3/2}$. Thus, the electron couples of Ni^{3+}/Ni^{2+} and V^{5+}/V^{4+} are coexisted in the orthorhombic $Ni_3V_2O_8$ structures, where the total atomic ratio of Ni and V elements is about 3:2, corresponding to the molecular formula of $Ni_3V_2O_8$.

The morphology structures of the as-synthesized $NH_4V_4O_{10}$ precursor and $Ni_3V_2O_8$ nanowire arrays are characterized by the FE-SEM technique, as shown in Fig. 2. Figure 2a,b show the top-view FE-SEM images of the $NH_4V_4O_{10}$ nanowire arrays. The precursor nanowires are distributed uniformly and adhered firmly to the surface of the Ti substrate. The inset in Fig. 2a is a digital image of the nanowire arrays on a Ti foil. The $NH_4V_4O_{10}$ nanowire arrays grow vertically on the substrate and can reach up to 6.2 μm, according to the cross-section FE-SEM view in Fig. 2c. After the second hydrothermal reaction, the surface of the aligned nanowires becomes rough, and the nanowires are changed to $Ni_3V_2O_8$ arrays, as shown in Fig. 2d–f, which are homogeneously aligned and separated apart. The length, diameter, and inter-wire space of $Ni_3V_2O_8$ nanowire arrays are about 6.8 μm (Fig. 2f), 321 nm (Fig. 2e), and 100 nm (Fig. 2e), respectively. Meanwhile, the second hydrothermal reaction of $NH_4V_4O_{10}$ and $C_4H_6O_4Ni$ with different reaction time is studied and the results are shown in Fig. S3. After 1 min reaction, the surfaces of the $NH_4V_4O_{10}$ nanowires become rough and the diameter of the nanowires are larger ($\sim$130 nm). 10 minute later, the diameter of the nanowires is about 260 nm and the nanowires are coated with nanosheets. When the reaction time is further extended to 2 h, the diameter is even larger and the wires are composed of
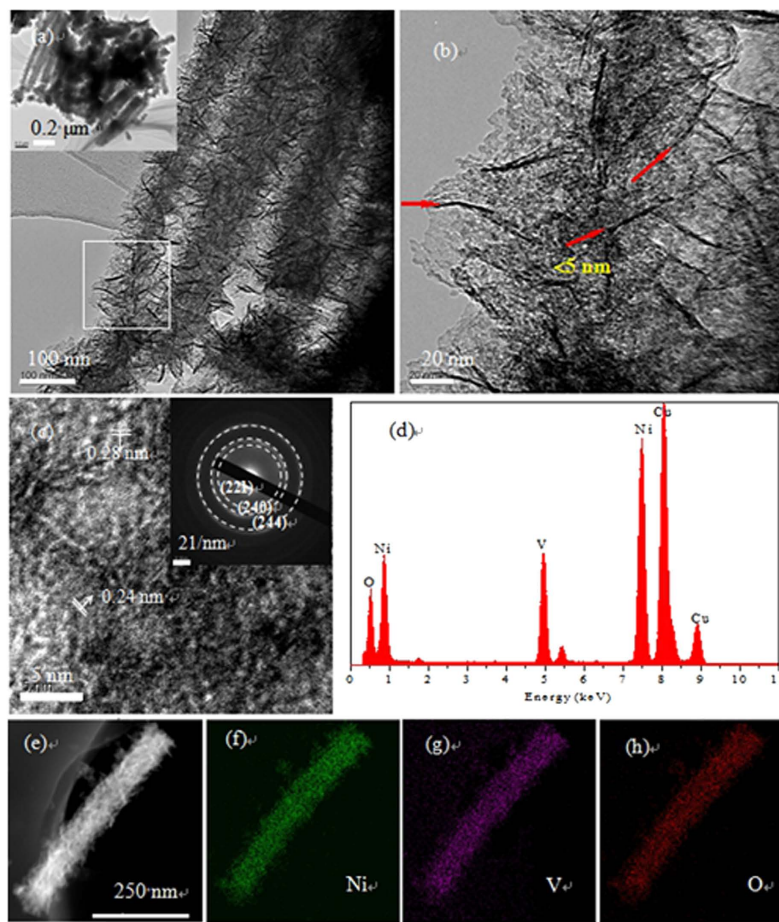
Figure 3. $Ni_3V_2O_8$ nanowire arrays scratched from Ti foil: (**a,b**) TEM image at different magnifications; (**c**) HR-TEM image (inset: SAED pattern); and (**d–h**) EDS maps of a single nanowire.

nanosheets. The corresponding schematic plot of the $Ni_3V_2O_8$ formation process is presented in Fig. S3e. During the extended reaction time, the $NH_4V_4O_{10}$ nanowires react with nickel salt from their surfaces to inners.

The morphology of the as-prepared $Ni_3V_2O_8$ nanowire arrays is further researched by TEM. Figure 3a shows a TEM image of an individual hybrid nanostructure in which $Ni_3V_2O_8$ nanowire arrays uniformly organized by ultrathin nanosheets. In addition, the thickness of the nanosheets is less than 5 nm from the contrast in the TEM image (Fig. 3b). The HR-TEM image shown in Fig. 3c reveals fringes with interplanar spacing of 0.24 nm and 0.28 nm, respectively, corresponding to the (131) and (115) plane of the orthorhombic $Ni_3V_2O_8$ (JCPDS card No. 70-1394). The selected area electron diffraction (SAED) pattern (the inset in Fig. 3c) indicates the polycrystalline nature of the $Ni_3V_2O_8$ nanosheets and the cycles can be readily indexed to (221), (240) and (244) crystal planes of the orthorhombic $Ni_3V_2O_8$ phase. An energy dispersive X-ray spectrometer (EDS) spectrum (Fig. 3d) shows that the atomic ratio of Ni/V/O is approximately 23.7/15.8/60.5, which is close to the ratio of Ni/V/O in the $Ni_3V_2O_8$ formula. The Cu signal in the spectrum is from Cu grid used during TEM characterization. Locations of the different elements are illustrated by element mapping: Ni (Fig. 3f), V (Fig. 3g), and O (Fig. 3h). It shows the entire nanowire is composed of Ni, V, and O elements, suggesting the formation of homogeneous $Ni_3V_2O_8$ nanowires.

After calcination at 300 °C, $Ni_3V_2O_8$ nanowires nearly keep their structure as shown in Fig. S4a. While the detail views in Fig. S4b,c present that the $Ni_3V_2O_8$ nanosheets transform into nanoparticles, which is further demonstrated by the TEM images as shown in Fig. S4d,e. The HR-TEM image shown in Fig. S4f reveals the interplanar spacing of 0.15 nm, corresponding to the (244) plane of the orthorhombic $Ni_3V_2O_8$. The SAED pattern (inset of Fig. S4f) also confirms that the nanoparticles are made of orthorhombic $Ni_3V_2O_8$. During heat treatment at 500 °C, the nanosheets on the wire will be curved to tubes (Fig. S5). As a result, the nanowire arrays organized by ultrathin nanosheets change to porous or tubular structures assembled by particles. In order to explain reason why the solid $Ni_3V_2O_8$ nanowires become tubular ones, the as-prepared samples were annealed at 500 °C with different time (Fig. S6). After 20 min, the nanosheets changed to wire-like structure. At 40 or 60 min, the wire-like structure further assembled to particle-like structure and this phenomenon is more obvious after 2 h. The corresponding schematic plot of the $Ni_3V_2O_8$ formation process is presented in Fig. S6e. The nanosheets assemble from their edge to central and forms wire-like structure. Further, the wire agglomerates from its two ends to central and form particle-like structure. The as-prepared $Ni_3V_2O_8$ nanosheets are assembled from single axles ($NH_4V_4O_{10}$ nanowires) (Fig. S3 in the support information), and therefore, the particles yielded from these nanosheets also

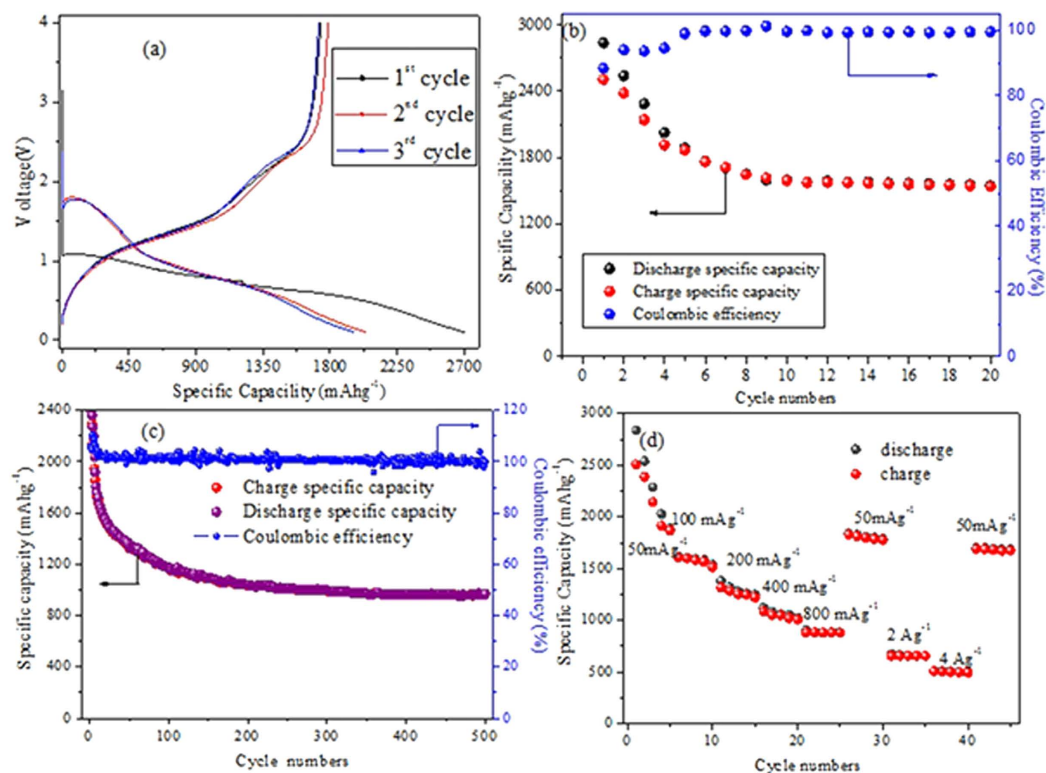**Figure 4.** Electrochemical lithium storage properties of as-prepared $Ni_3V_2O_8$ nanowire arrays on Ti foil: (**a**) the initial three charge/discharge voltage profiles at a constant current density of $50\,mA\cdot g^{-1}$; cycling performance at a current density of (**b**) $50\,mA\cdot g^{-1}$ or (**c**) $500\,mA\cdot g^{-1}$; and (**d**) rate performance at various current densities from $50\,mA\cdot g^{-1}$ to $4\,A\cdot g^{-1}$.

surrounded axially on the symcenters. The particles are at the geometric centrals of the original nanosheets, and if the particle size is ignored, the inner diameter of the tubular wires is about 1/2 radial length of the nanosheets.

The aligned $Ni_3V_2O_8$ nanowire arrays on Ti foil are evaluated as an electrode material for LIBs in view of their many appealing structural features. Fig. S7 shows the cyclic voltammogram (CV) plots of the first three cycles at a sweep rate of $0.1\,mV\,s^{-1}$ within a potential window of $0.1\text{–}4\,V$ (vs. Li/Li$^+$ ions). It can be seen that two pairs of redox peaks appear at 2.13/1.19 V and 2.77/2.41 V (vs. Li/Li$^+$ ions) for the as-prepared $NH_4V_4O_{10}$ nanowire arrays (Fig. S7a). The CV curves of the as-prepared $Ni_3V_2O_8$ nanowire arrays (Fig. S7b) and that annealed at at 300 °C (Fig. S7c) have a similar feature. In the first cathodic scan, a strong peak at 0.35–0.50 V can be detected corresponding to Faradaic redox reactions of the decomposition of active materials $Ni_3V_2O_8$ to Ni^0 ($Ni_3V_2O_8 + (6 + x)Li^+ + (6 + x)e^- \rightarrow 3Ni + Li_xV_2O_8 + 3Li_2O$). In the positive going potential scan, two obvious anodic peaks at 1.48 V and 2.44 V are observed, associated with the oxidation of Ni and the decomposition of $Li_xV_2O_8$, respectively[47]. Here, an irreversible capacity loss in the first cycle is caused by amorphous $Li_xV_2O_8$ producing and solid electrolyte interface (SEI) film forming. In the subsequent cycles, a peak at 0.55 V is observed corresponding to a reversible reaction of $Ni + Li_2O \leftrightarrow NiO + 2Li^+ + 2e^-$, and another peak at 1.52 V relates to the equation of $Li_xV_2O_8 + yLi^+ + ye^- \leftrightarrow Li_{x+y}V_2O_8$. In the subsequent cycles, the third cycle curve coincides with the second cycle well, indicating that the electrode reactions become more reversible.

The electrochemical performances of the as-prepared $Ni_3V_2O_8$ nanowire arrays for LIBs are also evaluated by galvanostatic discharge/charge test. All of the capacities in Fig. 4 are based on the whole mass of $Ni_3V_2O_8$ nanowire arrays with a cut-off voltage of $0.1\text{–}4\,V$ (versus Li/Li$^+$ ions). Figure 4a shows the initial three discharge/charge curves of the $Ni_3V_2O_8$ nanowire arrays at $50\,mA\cdot g^{-1}$, revealing the obvious platforms during the lithiation and delithiation processes. In the charge curve, we can see two potential plateaus located at 1.44 and 2.50 V, which correspond to the two oxidation peaks in the CV curve (Fig. S7). Another two potential plateaus are found in the discharge curve located at 0.57 and 1.62 V, agreeing with those reduction peaks in the CV curve. The initial discharge and charge capacities of the $Ni_3V_2O_8$ electrode are up to 2837.07 and 1706.76 mAh·g^{-1}, respectively. A specific capacity of 1545.53 mAh·g^{-1} can be remained after 20 cycles at $50\,mA\cdot g^{-1}$ (Fig. 4b). Further, the reversible capacity reaches 969.72 mAh·g^{-1} with a coulombic efficiency over 99% at $500\,mA\cdot g^{-1}$ (Fig. 4c) after 500 cycles, demonstrating the excellent cycling stability of the as-prepared $Ni_3V_2O_8$ nanowire arrays electrode. Impressively, our hierarchical $Ni_3V_2O_8$ nanowire arrays exhibit remarkably high-rate capability as shown in Fig. 4c. For each step, 5 cycles are measured to evaluate the rate performance. The average discharge capacities of the electrode at 50, 100, 200, 400, 800 mA·g^{-1}, 2 and 4 A·g^{-1} are 2315.01, 1585.52, 1296.73, 1065.34, 887.12, 662.26 and 502.81 mAh·g^{-1},

respectively (shown in Fig. 4d). It also reveals that after cycling at high-rate, the capacity can be recovered once the current density is returned back to $50\,mA\cdot g^{-1}$, implying excellent reversibility and rate capability. The multilevel hierarchical architecture based on nanosheet subunits and the hollow structure among the sheets offers a robust and porous framework, large electrode/electrolyte contact area, and reduced Li^+ ions diffusion distance, all of which benefit the electrochemical reaction kinetics in the electrode. On the other hand, such architecture can better withstand huge volume variation associated with repeated lithiation/delithiation process.

Figure S8a gives the cycle ability of the samples obtained at varieties temperatures (the as-prepared $Ni_3V_2O_8$ nanowire arrays and that annealed at 300 or 500 °C). It clearly shows that the as-prepared $Ni_3V_2O_8$ nanowire arrays can provide much higher capacities than that of their corresponding annealed samples, which is attributed to following reasons. After annealing at 300 or 500 °C, the $Ni_3V_2O_8$ nanosheets transform partly or totally into higher crystalline nanoparticles instead of the pure nanosheet structure. The self-assembled nanoparticals electrodes typically suffer from poor electrical conductivity due to the large interparticle spacing maintained, which will reduce the amount of active material taking part in electrochemical reaction and lower the lithium storage capacity[48].

For comparison, the cycling performances of $Ni_3V_2O_8$ nanowire arrays grown or pasted on Ti foil electrodes at a same current density ($300\,mA\cdot g^{-1}$) are shown in the Fig. S8b. It is observed that the $Ni_3V_2O_8$ nanowire arrays grown on the Ti foil electrode delivers a reversible capacity up to $1200.24\,mAh\cdot g^{-1}$ after 20 cycles. While, the reversible specific capacity of the $Ni_3V_2O_8$ nanowire arrays pasted on the Ti foil electrode reduces from $1505.82\,mAh\cdot g^{-1}$ to $911.51\,mAh\cdot g^{-1}$ during 20 cycles. It indicates that $Ni_3V_2O_8$ nanowire arrays grown on the Ti foil can make use of the advantages of special reinforcement properties to maintain the cycling reversibility and higher retention specific capacity. Electrochemical impedance spectroscopy (EIS) test is carried out to further understand the advantage of the $Ni_3V_2O_8$ nanowire arrays grown on the current collector (Ti foil) (Fig. S8c). $Ni_3V_2O_8$ nanowire arrays grown or pasted on Ti foil electrodes have the similar shapes of Nyquist plots, composed of a high-frequency semicircle and a long low-frequency subsequent 45° line. The black lines are the fitting curves by using the equivalent circuit, which is shown in the inset. It is made up of a parallel combination of a constant phase element (CPE), charge transfer resistance (Rp), Weber impedence (W), and solution resistance (Rs). The perfect semicircle was hardly achieved in this real system, thus, a CPE is used instead of a double-layer capacitance (C_{dl}). As shown in Table S2, the Rs of the $Ni_3V_2O_8$ electrodes changes from $6.16\,\Omega$ (grown on Ti foil) to $15.70\,\Omega$ (pasted on Ti foil), manifesting a good conductivity of the electrolyte and the lower ionic and electronic resistance of the nanowires grown on Ti foil. A schematic in Fig. S8d presents charge storage mechanism of the $Ni_3V_2O_8$ nanowire array electrode. In the discharge process, electrons will pass through the contact point of the nanowires and the titanium substrate, and then up along the nanowires. Li^+ ions can migrate in the electrolyte, reach the electrode, and take part in the electrochemical reaction with $Ni_3V_2O_8$. In the charge process, the movements of the Li^+ ions and electrons are reverse. By growing directly from the $NH_4V_4O_{10}$ nanowire scaffold, $Ni_3V_2O_8$ nanowire arrays organized by ultrathin nanosheets are well separated, making them fully available to the Li^+ ions in the electrolyte. The directly grown nanowire arrays can ensure good mechanical adhesion and electrical connection to the current collector, which avoids extra contact resistance.

For comparison, a cut-off voltage of 0.1–3.0 V (versus Li/Li^+) was selected during carrying out the electrochemical properties of the $Ni_3V_2O_8$ nanowire arrays growing on Ti foil. The electrochemical properties are shown in Fig. S9. Figure S9a shows the CV plots of the first three cycles at a sweep rate of $0.1\,mV\,s^{-1}$ within a potential window of 0.1–3.0 V (vs. Li/Li^+) and the peak positions are similar to that obtained with a cut-off voltage of 0.1–4.0 V (versus Li/Li^+). The initial three charge/discharge voltage profiles at a constant current density of $50\,mA\cdot g^{-1}$ within a potential window of 0.1–3.0 V (vs. Li/Li^+) are shown in Fig. S9b. Further, a specific capacity of $1389.57\,mAh\cdot g^{-1}$ is remained at the current densities of $50\,mA\cdot g^{-1}$ after 20 cycles (Fig. S9c) or $890.89\,mAh\cdot g^{-1}$ at the current densities of $500\,mA\cdot g^{-1}$ after 500 cycles (Fig. S9d). Further, the morphology stability of the sample after 50 cycles are tested and presented in Fig. S10. The overall wire structures can be generally retained, although the detailed nanosheet structures become somewhat diminished and thicken. This is understandable, as these nanosheets might be too thin and large to withstand the high-rate insertion/extraction of lithium ions over extended cycling[49]. Further, the volume expansion will occur after lithium ion insertion, therefore, the nanosheets broaden after galvanostatic charge-discharge cycling.

Conclusion

In summary, we demonstrated, for the first time, a new type of $Ni_3V_2O_8$ nanowire arrays organized by ultrathin nanosheets obtained by a two-step hydrothermal synthesis method on a Ti substrate. In virtue of the structural advantages, the obtained $Ni_3V_2O_8$ nanowire arrays manifest excellent electrochemical properties as potential anode materials for LIBs in terms of high specific capacity, remarkable cycling ability, and superior rate capability. In our case, the superior electrochemical performances of $Ni_3V_2O_8$ nanowire arrays result from the following factors: (i) uniform nanosized sheets, decreasing the electrochemical polarization; (ii) hierarchical structure, providing shortened Li^+ ions/electron diffusion pathways and relieving to the volume changes during cycling; (iii) high structural stability, preventing the nanomaterials from dissolving into electrolyte; (iv) nanowire arrays on the current collector (Ti foil), enabling the active roles of nanowires in electrode reactions to benefit the transitions of ions and electrons. The present work indicates that the experimentally designed $Ni_3V_2O_8$ nanowire arrays possesses great application potentials in high-performance energy storage devices, and this method may be extended for other transition metal oxides for the development of lithium ion batteries.

Methods

Synthesis Material. First, self supported $NH_4V_4O_{10}$ nanowire arrays are prepared by a facile hydrothermal synthesis method. The solution is prepared by ultrasonic dissolving ammonium metavanadate (NH_4VO_3), oxalic acid ($H_2C_2O_4\cdot 2H_2O$), and hexamethylene tetramine ($C_6H_{12}N_4$) in distilled water. The Ti foil as the substrate

(1 cm in diameter) is immersed into the reaction solution. Then, this resulting solution is transferred into Teflon-lined stainless steel autoclave liners and heated to 150 °C for 40 min inside a conventional laboratory oven. Subsequently, the sample is rinsed with distilled water and dried at 50 °C to obtain a $NH_4V_4O_{10}$ nanowire array on Ti foil. To fabricate $Ni_3V_2O_8$ nanowire arrays, a piece of Ti substrate covered with the $NH_4V_4O_{10}$ nanowire array is used as the scaffold for $Ni_3V_2O_8$ nanoflake growth. The nickel acetate ($C_4H_6O_4Ni$) aqueous solution is prepared by stirring dissolving $C_4H_6O_4Ni$ in distilled water. Then the $NH_4V_4O_{10}$ nanowire arrays on Ti foil are put into a Teflon-lined stainless steel autoclave containing the nickel acetate aqueous solution as mentioned above at 120 °C for 2 h. Finally, the sample is removed, washed with distilled water and dried at 50 °C to obtain the $Ni_3V_2O_8$ nanowire arrays organized by ultrathin nanosheets. For comparison, the as-prepared $Ni_3V_2O_8$ nanowire arrays are annealed at 300 or 500 °C in air.

Material Characterization. The samples are characterized by X-ray diffraction (XRD, RIGAKUD/Max-2550 with Cu Kα radiation), Energy dispersive X-ray spectrometer (EDS), Field emission scanning electron microscopy (FE-SEM, JSM-6700F at 160 kV), Transmission electron microscopy (TEM, Tecnai G220ST at 200 kV), and High resolution transmission electron microscopy (HR-TEM). The chemical composition of the sample is analyzed by X-ray photoelectron spectroscopy (XPS, Kα 1063, Thermo Fisher Scientific, UK).

Electrochemical Characterization. Electrochemical analyses are performed using coin-type cells (CR2016) with lithium metal as the negative electrode, which are assembled in an argon-filled glove box at room temperature. The Ti substrates supported $NH_4V_4O_{10}$ nanowire arrays, $Ni_3V_2O_8$ (as-prepared) nanowire arrays and that annealed at 300 °C or 500 °C are directly used as the positive electrode without any binders or conducting additives. For comparison, the electrode slurry of the $Ni_3V_2O_8$ nanowire powder is prepared by mixing the active material detached from Ti substrate using a knife, acetylene black (AB) and polyvinylidene fluoride (PVDF) with a weight ratio of 8:1:1. The resulting slurry is pasted onto a Ti foil, which is used as the current collector. The electrolyte is 1 M $LiPF_6$ in ethylene carbonate (EC)/diethyl carbonate (DEC) (1:1, v/v). Cyclic voltammetry (CV) measurements are performed on a CHI660 electrochemical workstation in the voltage range of 0.1–4 V at a scanning rate of 0.1 mV s^{-1}. The galvanostatic discharge/charge tests are conducted on a LAND battery program-control test system at different current densities in the voltage range of 0.1–4 V. Electrochemical impedance spectroscopy (EIS) is measured at an open voltage using a PGSTAT 302N electrochemical workstation (Autolab) in the frequency range of 0.01 Hz–5 kHz.

References

1. Tarascon, J. M. & Armand, M. Issues and challenges facing rechargeable lithium batteries. *Nature* **414,** 359–367 (2001).
2. Patil, A. *et al.* Issue and challenges facing rechargeable thin film lithium batteries. *Mater. Res. Bull.* **43,** 1913–1942 (2008).
3. Cheng, F. *et al.* Functional materials for rechargeable batteries. *Adv. Mater.* **23,** 1695–1715 (2011).
4. Jeong, G. *et al.* Prospective materials and applications for Li secondary batteries. *Energy Environ. Sci.* **4,** 1986–2002 (2011).
5. Song, J. *et al.* The reversible anomalous high lithium capacity of MnO_2 nanowires. *Chem. Commun.* **50,** 7352–7355 (2014).
6. Fang, D. *et al.* Self-assembled hairy ball-like Co_3O_4 nanostructures for lithium ion batteries. *J. Mater. Chem. A* **1,** 13203–13208 (2013).
7. Fang, D. *et al.* Self-assembled hairy ball-like V_2O_5 nanostructures for lithium ion batteries. *RSC Adv.* **4,** 25205–25209 (2014).
8. Wang, D. H. *et al.* Hierachical mesoporous silica wires by confined assembly. *Chem. Commun.* **2,** 166–167 (2005).
9. Bruce, P. G. *et al.* Nanomaterials for rechargeable lithium batteries. *Angew. Chem. Int. Ed.* **47,** 2930–2946 (2008).
10. Rolison, D. R. *et al.* Multifunctional 3D nanoarchitectures for energy storage and conversion. *Chem. Soc. Rev.* **38,** 226–252 (2009).
11. Kang, B. *et al.* Battery materials for ultrafast charging and discharging. *Nature* **458,** 190–193 (2009).
12. Chung, S. Y. *et al.* Electronically conductive phospho-olivines as lithium storage electrodes. *Nat. Mater.* **1,** 123–128 (2002).
13. Wang, Y. *et al.* The design of a LiFePO$_4$/carbon nanocomposite with a core–shell structure and its synthesis by an *in situ* polymerization restriction method. *Angew. Chem. Int. Ed.* **47,** 7461–7465 (2008).
14. Wang, Y. *et al.* Nanostructured vanadium oxide electrodes for enhanced lithium-ion intercalation. *Adv. Funct. Mater.* **16,** 1133 (2006).
15. Kim, M. G. *et al.* Reversible and High-Capacity Nanostructured Electrode Materials for Li-Ion Batteries. *Adv. Funct. Mater.* **19,** 1497–1514 (2009).
16. Hu, Y. S. *et al.* Synthesis and Electrode Performance of Nanostructured V_2O_5 by Using a Carbon Tube-in-Tube as a Nanoreactor and an Efficient Mixed-Conducting Network. *Angew. Chem. Int. Ed.* **48,** 210–214 (2009).
17. Singhal, A. *et al.* Nanostructured electrodes for next generation rechargeable electrochemical devices. *J. Power Sources* **129,** 38–44 (2004).
18. Fang, X. *et al.* Enhanced Li storage performance of ordered mesoporous MoO_2 via tungsten doping. *Nanoscale* **4,** 1541–1544 (2012).
19. Guo, Y. G. *et al.* Synthesis of hierarchically mesoporous anatase spheres and their application in lithium batteries. *Chem. Commun.* 2783–2785 (2006).
20. Chen, S. *et al.* Self-supported $Li_4Ti_5O_{12}$ nanosheet arrays for lithium ion batteries with excellent rate capability and ultralong cycle life. *Energy Environ. Sci.* **7,** 1924–1930 (2014).
21. Li, L. L. *et al.* A Flexible Quasi-Solid-State Asymmetric Electrochemical Capacitor Based on Hierarchical Porous V_2O_5 Nanosheets on Carbon Nanofibers. *Adv. Energy Mater.* (2015), Available at: http://onlinelibrary.wiley.com/doi/10.1002/aenm.201500753/full. (Accessed: 1st July 2015).
22. Wu, H. B. *et al.* Nanostructured metal oxide-based materials as advanced anodes for lithium-ion batteries. *Nanoscale* **4,** 2526–2542 (2012).
23. Yuan, C. *et al.* Mixed Transition-Metal Oxides: Design, Synthesis, and Energy-Related Applications. *Angew. Chem. Int. Ed.* **53,** 1488–1504 (2014).
24. Xia, X. H. *et al.* Freestanding Co_3O_4 nanowire array for high performance supercapacitors. *Rsc Adv.* **2,** 1835–1841 (2012).
25. Sato, H. *et al.* Transparent conducting p-type NiO thin films prepared by magnetron sputtering. *Thin Solid Films* **236,** 27–31 (1993).
26. Kang, W. P. *et al.* High interfacial storage capability of porous $NiMn_2O_4$/C hierarchical tremella-like nanostructures as the lithium ion battery anode. *Nanoscale* **7,** 225–231 (2015).
27. Mondal, A. K. *et al.* Highly porous $NiCo_2O_4$ nanoflakes and nanobelts as anode materials for lithium-ion batteries with excellent rate capability. *ACS Appl. Mat. Interfaces* **6,** 14827–14835 (2014).
28. Wei, T. Y. *et al.* A cost-effective supercapacitor material of ultrahigh specific capacitances: spinel nickel cobaltite aerogels from an epoxide-driven sol-gel process. *Adv. Mater.* **22,** 347 (2010).

29. Afyon, S. *et al.* New High Capacity Cathode Materials for Rechargeable Li-ion Batteries: Vanadate-Borate Glasses. *Scientific reports* **4,** 7113 (2014).
30. Armstrong, A. R. *et al.* The lithium intercalation process in the low-voltage lithium battery anode $Li_{1+x}V_{1-x}O_2$. *Nat. Mater.* **10,** 223–229 (2011).
31. Sim, D. H. *et al.* Direct growth of $FeVO_4$ nanosheet arrays on stainless steel foil as high-performance binder-free Li ion battery anode. *RSC Adv.* **2,** 3630–3633 (2012).
32. Soudan, P. *et al.* The sol-gel mixed oxide $Cr_{0.11}V_2O_{5.16}$: An attractive cathodic material for secondary lithium batteries. *Ionics* **3,** 261–264 (1997).
33. Cao, Y. *et al.* Novel aligned sodium vanadate nanowire arrays for high-performance lithium-ion battery electrodes. *RSC Adv.* **5,** 42955–42960 (2015).
34. Spahr, M. E. *et al.* Characterization of layered lithium nickel manganese oxides synthesized by a novel oxidative coprecipitation method and their electrochemical performance as lithium insertion electrode materials. *J. Electrochem. Soc.* **145,** 1113–1121 (1998).
35. Xia, X. H. *et al.* High-quality metal oxide core/shell nanowire arrays on conductive substrates for electrochemical energy storage. *ACS Nano* **6,** 5531–5538 (2012).
36. Liu, J. *et al.* Co_3O_4 Nanowire@ MnO_2 Ultrathin Nanosheet Core/Shell Arrays: A New Class of High-Performance Pseudocapacitive Materials. *Adv. Mater.* **23,** 2076–2081 (2011).
37. Liu, M. C. *et al.* Synthesis and characterization of $M_3V_2O_8$ (M= Ni or Co) based nanostructures: a new family of high performance pseudocapacitive materials. *J. Mater. Chem. A* **2,** 4919–4926 (2014).
38. Singh, A. K. *Advanced x-ray techniques in research and industry*, 307–315 (Amsterdam, 2005).
39. Kandemir, T. *et al.* Microstructural and defect analysis of metal nanoparticles in functional catalysts by diffraction and electron microscopy: The Cu/ZnO catalyst for methanol synthesis. *Top. Catal.* **57,** 188–206 (2014).
40. Patterson, A. L. The Scherrer formula for X-ray particle size determination. *Phys. Rev.* **56,** 978 (1939).
41. Zhao, Y. *et al.* Microstrain and grain-size analysis from diffraction peak width and graphical derivation of high-pressure thermomechanics. *Appl. Cryst.* **41,** 1095–1108 (2008).
42. Rogado, N. *et al.* The Kagomé-staircase lattice: magnetic ordering in $Ni_3V_2O_8$ and $Co_3V_2O_8$. *Solid State Commun.* **124,** 229–233 (2002).
43. McIntyre, N. S. *et al.* X-ray photoelectron studies on some oxides and hydroxides of cobalt, nickel, and copper. *Anal. Chem* **47,** 2208–2213 (1975).
44. Shi, Q. *et al.* Giant phase transition properties at terahertz range in VO_2 films deposited by sol–gel method. *ACS Appl. Mat. Interfaces* **3,** 3523–3527 (2011).
45. Reddy, B. M. *et al.* Surface characterization of La_2O_3-TiO_2 and V_2O_5/La_2O_3-TiO_2 catalysts. *J. Mater. Chem. B* **106,** 5695–5700 (2002).
46. Yang, X. *et al.* Mixed phase titania nanocomposite codoped with metallic silver and vanadium oxide: new efficient photocatalyst for dye degradation. *J. Hazard. Mater.* **175,** 429–438 (2010).
47. Yang, G. *et al.* Self-assembly of $Co_3V_2O_8$ multilayered nanosheets: controllable synthesis, excellent Li-storage properties, and investigation of electrochemical mechanism. *ACS Nano* **8,** 4474–4487 (2014).
48. Dong, A. *et al.* Electronically coupled nanocrystal superlattice films by *in situ* ligand exchange at the liquid–air interface. *ACS Nano* **7,** 10978–10984 (2013).
49. Chen, J. S. *et al.* Constructing hierarchical spheres from large ultrathin anatase TiO_2 nanosheets with nearly 100% exposed (001) facets for fast reversible lithium storage. *J. Am. Chem. Soc.* **132,** 6124–6130 (2010).

Acknowledgements

Author Contributions

D.F. designed experiments; C.W. and Y.H.C. carried out experiments; H.E.W., X.Q.L., G.Z.L. analyzed experimental results; Z.P.L., M.J. and C.X.X. analyzed sequencing data and developed analysis tools; W.L.X. assisted with Illumina sequencing. C.W. and D.F. wrote the manuscript.

Additional Information

Supplementary information accompanies this paper at http://www.nature.com/srep

Competing financial interests: The authors declare no competing financial interests.

How to cite this article: Wang, C. *et al.* Uniform Nickel Vanadate ($Ni_3V_2O_8$) Nanowire Arrays Organized by Ultrathin Nanosheets with Enhanced Lithium Storage Properties. *Sci. Rep.* **6,** 20826; doi: 10.1038/srep20826 (2016).